PNAS RESEARCH ARTICLE | PHYSICS OPEN ACCESS

Nonequilibrium topological spin textures in momentum space

Xiao-Xiao Zhang[a,1] and Naoto Nagaosa[a,b,1]

Contributed by Naoto Nagaosa; received September 15, 2021; accepted February 14, 2022; reviewed by A. Cavalleri and P. Werner

Nonequilibrium quantum dynamics of many-body systems is the frontier of condensed matter physics; recent advances in various time-resolved spectroscopic techniques continue to reveal rich phenomena. Angle-resolved photoemission spectroscopy (ARPES) as one powerful technique can resolve electronic energy, momentum, and spin along the time axis after excitation. However, dynamics of spin textures in momentum space remains mostly unexplored. Here, we demonstrate theoretically that the photoexcited surface state of genuine or magnetically doped topological insulators shows intriguing topological spin textures (i.e., tornado-like patterns) in the spin-resolved ARPES. We systematically reveal its origin as a unique nonequilibrium photoinduced topological winding phenomenon. As all intrinsic and extrinsic topological helicity factors of both material and light are embedded in a robust and delicate manner, the tornado patterns not only allow a remarkable tomography of such important system information, but also enable various unique dichroic topological switchings of the momentum-space spin texture. These results open a direction of nonequilibrium topological spin states in quantum materials.

topology | spin textures | tornado | angle-resolved photoemission | nonequilibrium

The recent decade has witnessed significant advances in the detection means of ultrafast light-induced phenomena (1, 2) in terms of time-resolved spectroscopic techniques, including angle-resolved photoemission spectroscopy (ARPES) (3–5), terahertz pump-probe scanning–tunneling microscopy, optical conductivity measurement (6–9), etc. Unprecedented precise access into the inherently time-dependent phenomena is beneficial and important to both the fundamental interest in nonequilibrium physics and the practical connection to ultrafast manipulation of novel quantum degrees of freedom toward application (10–12). To this end, a robust low-dimensional nontrivial system would be a versatile playground for such surface-sensitive pump-probe–type investigations. The protected surface state of the topological insulator fits into this role for its long-enough mean free path and lifetime and also, for excluding the insulating and spin-degenerate bulk influence (13–15). The tunable exchange gap from controlling magnetic doping further allows for demonstrating both massless and massive Dirac physics (16–19).

However, nonequilibrium spin dynamics is usually studied in time domain or real space only (20, 21). For the surface state, it has been focused on the equilibrium spin-orbit coupling features (22, 23) and the photo-driven steady-state or highly pumped charge current responses (24–29). The nonequilibrium phenomena of light–matter interaction in this system remain largely buried partially due to the little appreciated spin-channel physics. In fact, such information connects well to the state-of-the-art experimental reach; for example, spin-resolved angle-resolved photoemission spectroscopy (SARPES) has been established in equilibrium and as well, extended to time-dependent measurement well below picosecond resolution (5, 22, 23, 30–34). As an example of the new front of nonequilibrium quantum dynamics of topological matters, we draw attention to this highly informative time-dependent signal in an optical pump-probe experiment upon the surface state.

In particular, we simulate the irradiation of a terahertz short laser pulse, which can be either linearly polarized (LP) or circularly polarized (CP) (35), to pump across the exchange gap and then, detect the SARPES signal after a controllable delay time with a probe pulse. Apart from possible resonant transition, virtual excitation at the early stage of time evolution is a purely quantum mechanical effect and can turn the system into a many-particle coherent nonequilibrium state. Surprisingly, the SARPES signal exhibits robust and topological tornado-like spiral structures in the two-dimensional (2D) momentum $\boldsymbol{k}$ space, which can be characterized by topological indices. This happens in both the normal and in-plane spin channels and embeds a delicate relation to three helicity factors determining the pumped system: intrinsic helicity of the surface state $\chi = \pm 1$, sign of the Dirac mass $\nu = \mathrm{sgn}(m)$, and extrinsic helicity $\tau = 0, \pm 1$ for LP and right or left CP lights, respectively. Depending on these, the tornado-like responses can dichotomously change characteristic winding senses and even dichroically switch between topological and trivial as a $\mathbb{Z}_2$-like topological optical activity.

Significance

Optically excited systems can host unprecedented phenomena and reveal key information. The spin-channel physics in the photoexcited dynamics of quantum matter remains largely unexplored. This study finds the topological surface state under contemporary time-resolved pump-probe spectroscopy an exceptionally capable platform in this regard. Spin signals exhibit interesting tornado-like spiral patterns, and the unusual topological optical activity can be indicative of spintronic applications. This exemplifies a purely nonequilibrium topological winding phenomenon, where all the hidden helicity factors in the light–matter-coupled system are robustly encoded. These results open a direction of nonequilibrium topological spin states in quantum materials.

Author affiliations: [a]RIKEN Center for Emergent Matter Science (CEMS), Saitama 351-0198, Japan; and [b]Department of Applied Physics, The University of Tokyo, Tokyo 113-8656, Japan

Author contributions: N.N. designed research; X.-X.Z. performed research; X.-X.Z. and N.N. analyzed data; and X.-X.Z. and N.N. wrote the paper.

Reviewers: A.C., Max Planck Institute for the Structure and Dynamics of Matter; and P.W., Fribourg University.

The authors declare no competing interest.

[1]To whom correspondence may be addressed. Email: xiaoxiao.zhang@riken.jp or nagaosa@ap.t.u-tokyo.ac.jp.

This article contains supporting information online at https://www.pnas.org/lookup/suppl/doi:10.1073/pnas.2116976119/-/DCSupplemental.

Published March 18, 2022.

Results

Model and Time Evolution. We consider the 2D massive Dirac model and henceforth, set $\hbar = 1$ and

$$H_0(\boldsymbol{k}) = \boldsymbol{d}(\boldsymbol{k}) \cdot \boldsymbol{\sigma} = v(k_x\sigma_2 - \chi k_y \sigma_1) + m\sigma_3 \quad [1]$$

to represent the surface state with spin Pauli matrices $(\sigma_0, \boldsymbol{\sigma}) = (I, \sigma_1, \sigma_2, \sigma_3)$. We include the $\chi = -1$ case possible when $C_{n>2}$ rotational symmetries are broken. The two bands $\varepsilon_{\boldsymbol{k}\pm} = d_0(k) \pm d(\boldsymbol{k})$ if we include the spin-independent quadratic term $d_0(k)\sigma_0$, which is henceforth dropped as it does not affect spin-channel response from interband transitions. The hexagonal warping strength c_6 measured in the dimensionless quantity $c_6 k_0^2/v \ll 1$ makes it negligible with the characteristic wave number k_0 introduced later (36, 37). Therefore, our prediction is fully based on the leading order response in real systems. The ARPES light source typically bears a beam spot size 10 to 100 μm upon the sample (1, 5, 35, 38), which requests one to consider physical phenomena at the optical long-wavelength limit as the experimentally most relevant scenario, in contrast to the otherwise interesting space-resolved nano-ARPES or scanning Kerr magnetooptic microscopy study (39–41). We thus introduce a spatially uniform Gaussian vector potential for the pump pulse vertically shone onto the *xy* plane $\boldsymbol{A}(t) = A_0 \exp(-t^2/2t_0^2)\,[\hat{x}\cos\Omega t + \tau\,\hat{y}\sin\Omega t]$, where $\tau = 0, \pm 1$ and t_0 is the temporary width. The conserved momentum enables us to derive the full electromagnetically coupled Hamiltonian from Peierls substitution

$$\hat{H}(t) = \sum_{\boldsymbol{k}} \psi^\dagger(\boldsymbol{k})\,[H_0(\boldsymbol{k}) + e\partial_{\boldsymbol{k}} H_0(\boldsymbol{k}) \cdot \boldsymbol{A}(t)]\,\psi(\boldsymbol{k}) \quad [2]$$

with $\psi(\boldsymbol{k}) = (\psi_{\boldsymbol{k}\uparrow}, \psi_{\boldsymbol{k}\downarrow})^{\mathrm{T}}$. The time-dependent spinor operator $\psi_{\boldsymbol{k}\alpha}(t)$ for $\alpha = \uparrow / \downarrow$ can be obtained via the equation of motion (EOM), which relates to the double–time matrix removal Green's function with nonequilibrium occupation and excitation information $G^<_{\alpha\beta}(\boldsymbol{k}, t_1, t_2) = \mathrm{i}\langle\psi^\dagger_{\boldsymbol{k}\beta}(t_2)\psi_{\boldsymbol{k}\alpha}(t_1)\rangle$ (42, 43) (*Materials and Methods*).

Time-Dependent SARPES Signal. We generalize the time-resolved ARPES theory to obtain the time-dependent SARPES intensity matrix (44, 45) $P(\varepsilon, \boldsymbol{k}, t) = -\mathrm{i}\int \mathrm{d}t_1 \mathrm{d}t_2\, \mathrm{e}^{\mathrm{i}\varepsilon(t_1 - t_2)} s(t_1 - t)\, s(t_2 - t)\, G^<(\boldsymbol{k}, t_1, t_2)$, with $s(t) = (2\pi t_{\mathrm{pb}}^2)^{-\frac{1}{2}} \mathrm{e}^{-t^2/2t_{\mathrm{pb}}^2}$ the isotropic probe pulse of width t_{pb} and the spin-polarized photocurrent intensity $I_\alpha \propto P_{\alpha\alpha}$ (*SI Appendix*, note 1). Then, we define

$$P_i(\varepsilon, \boldsymbol{k}, t) = \mathrm{Tr}[\sigma_i P(\varepsilon, \boldsymbol{k}, t)], \qquad i = 0, 1, 2, 3 \quad [3]$$

successively for the density and three spin channels to be our main focus since the SARPES polarization reads (e.g., for *z* direction) $\mathrm{P}_z = \frac{I_\uparrow - I_\downarrow}{I_\uparrow + I_\downarrow} = \frac{P_3}{P_0}$. As we mainly consider a probe pulse well separated from the pump pulse ($t \gg t_0$), we can stick to the present Hamiltonian gauge and are free from gauge invariance issues (46, 47).

The pump field renders the original Dirac bands no longer eigenstates, and occupation can in general change; in the $(\varepsilon, \boldsymbol{k})$ hyperplane, not only on-resonance real transition can happen when the gap $\Delta = 2m < \Omega$, which is the case shown in Fig. 1, but also, off-resonance virtual excitations significantly contribute, constituting a transient redistribution along the ε axis per the particle conservation as a sum rule–like constraint. After the pump field fully decays, Dirac bands return to be eigenstates. For the density channel, shown in Fig. 1 *A*, a1, *B*, b1, and *C*, c1, this implies that, except for resonant interband transition, the signal should mostly become stable after the pumping transients. However, in the spin channel, pumping has already left relics of light–matter interaction. Each momentum accommodates a two-level system and is subject to the common photoexcitation. This leads to a highly nontrivial correlation of excited spin orbit–coupled states in $\boldsymbol{k}$ space as the central cause of the SARPES tornado textures discussed below. Indeed, collective quantum oscillation effect can emerge near some hot region in the $(\varepsilon, \boldsymbol{k})$ hyperplane of SARPES, centered at the band midpoint as shown in Fig. 1 *B*, b2–b4 and *C*, c2–c4). This is because the spin channel extracts the Rabi-like oscillatory information due to interband coherence even as $\hat{H}$ loses time dependence after the pump pulse. Note also that, as is physically originated from the spin-channel interband quantum oscillation, the real resonant pumping, if any, is insignificant for the hot region signals, which will also become clear later with the analytical result Eq. **6**.

The probe pulse width t_{pb} is a double-edged sword per the uncertainty relation; smaller t_{pb} gives better time resolution but less energy resolution and vice versa. It thus broadens the transient process and smears the SARPES energy levels. Furthermore, a certain amount of relaxed energy conservation $\delta\varepsilon \sim 2\pi/t_{\mathrm{pb}}$ and the associated momentum range $\delta k \propto \delta\varepsilon/v$ can actually enhance the signal from off-resonance oscillations and provide the hot region characteristic scales because energy-sharp bands are incapable of capturing the quantum oscillations. Certainly, too poor energy resolution would otherwise mix contributions, for instance, from both the lower band and the possible higher occupation due to resonant transition. We also emphasize that this quantum nonequilibrium phenomenon goes beyond the semiclassical picture (48); neither the pumping process nor the interband coherent dynamics at any time can be captured by the wave packet description within a single band. Direct evidence is the anomalous tornado rotation as the quasiparticle trajectory, which is otherwise not expected after the driving electric field in the pump pulse dies out.

Nonequilibrium Tornado Responses. The most interesting information lies in the $\boldsymbol{k}$-space spin texture $\boldsymbol{P}(\varepsilon, \boldsymbol{k}, t) = (P_1, P_2, P_3)$ within an energy slice in the hot region, where robust tornado-like structures widely appear as shown in Fig. 2 (*SI Appendix*, Figs. S1–S3 show cases with different χ, ν). Such an energy-momentum hot region lies in general away from where resonant real transitions happen since the tornado mainly originates from coherent virtual excitations, which will be seen also from analytical results. As aforementioned, there are three helicity factors χ, ν, τ at play during the light–matter interaction, for which the subsequent nonequilibrium tornado response turns out to be an exceptionally apt and reliable bookkeeper. For any tornado pattern, one can intuitively identify the rotation sense helicity $\Xi_s = \pm 1$ of the spiral and the number $\mathcal{R}_s$ of repeating spiral arms. Practically, $\Xi_s = \mathrm{sgn}[\partial k^*/\partial\theta_{\boldsymbol{k}}]$ with $\theta_{\boldsymbol{k}}$ the azimuthal angle of $\boldsymbol{k}$ and $k^*(\theta_{\boldsymbol{k}})$ any polar-coordinate contour line in a spiral arm. These two lead to the universal topological spiral winding number

$$W_s = \Xi_s \mathcal{R}_s. \quad [4]$$

We exemplify these quantities in Fig. 3. For the in-plane orientation $\phi(\boldsymbol{k}) = \tan^{-1} \boldsymbol{P}_{\mathrm{in}}(\boldsymbol{k})$ of the vector field $\boldsymbol{P}_{\mathrm{in}} = (P_1, P_2)$, W_s is readily determined by a combination of ϕ 's radial and azimuthal variations. $\phi(\boldsymbol{k})$ has a definite ordering, $\mathcal{K} = \mathrm{sgn}(\partial_k \phi)$ (i.e., the rainbow order along the radius in our illustration). The latter is encoded in a topological circular winding number

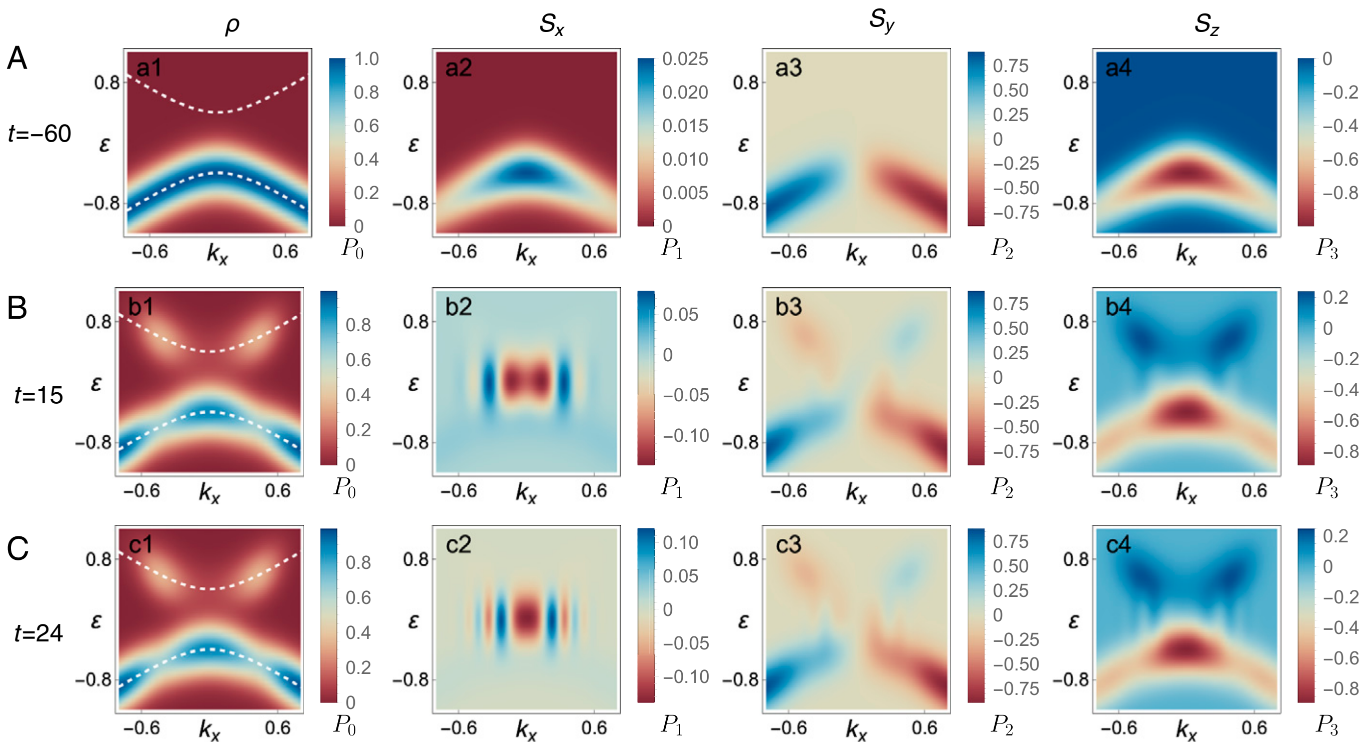

Fig. 1. Nonequilibrium SARPES signals in the (ε, k_x) plane. P_0, P_1, P_2, P_3 successively in the density ρ and spin $\boldsymbol{S}$ channels of a magnetic topological insulator surface state at three different times. White dashed curves in *A*, a1, *B*, b1, and *C*, c1 indicate the surface-state band dispersion. The band broadening originates from finite probe pulse width. Parameters are $\chi = \tau = 1, t_0 = t_{\mathrm{pb}} = 3, \Omega = 1.2, v = 1, m = 0.4, A_0 = 0.1, k_y = 0.01, \beta = 50, \mu = 0, e = \hbar = k_B = 1$. (*A*) The $t = -60$ signal before pump pulse irradiation exhibits equilibrium response; only the lower band is visible due to the relatively low temperature specified by $\beta = 1/(k_B T)$ and in-gap chemical potential. The 90° out-of-phase spin-momentum locking manifests in the spin channels. P_1 is weak compared with others due to small k_y. P_2 reverses sign between positive and negative k_x axes. P_3 is made finite purely by the finite exchange gap. (*B*) At $t = 15$ after the pump pulse centered at $t = 0$ almost fully decays, resonant real transition appears as two spots in the upper band in P_0. The spin channels exhibit a signal hot region centered at $\varepsilon = 0$ and $k_x = 0$, which is oscillatory in time and momentum. This is clearly seen in P_1 for the weak background from real band occupations, compared with P_2, P_3. (*C*) At a later time $t = 24$, while the density channel remains nearly time independent after the pumping process, the hot region signals in the spin channel evolve in time with increasing fine structures, implying that it originates mainly from virtual excitations and the coherent quantum oscillation correlated in momentum space.

$$w_\phi = \frac{1}{2\pi}\int_{C_k} \mathrm{d}\boldsymbol{k}\cdot\nabla\phi(\boldsymbol{k}) \qquad [5]$$

along a counterclockwise circle C_k of any radius k in the 2D $\boldsymbol{k}$ plane. We hence obtain $W_s = -\mathcal{K}w_\phi$. Note that, depending on the helicity factors, any two of $\mathcal{K}, w_\phi, W_s$ can switch signs independently, and the two together determine the topological tornado features. On the other hand, for a scalar field with less information, P_3, or the amplitude $|\boldsymbol{P}_{\mathrm{in}}|$, only Eq. **4** is relevant and suffices to specify the tornado pattern, which will later be cast in the same form as Eq. **5** from the analytical result.

Table 1 summarizes the correspondence between the three helicity factors and five related aspects in P_3 and $\boldsymbol{P}_{\mathrm{in}}$. The dichroic strong/weak response strength of P_3 happens with CP light and can be owed to the dipole interband matrix element $\langle\pm|\hat{\boldsymbol{v}}|\mp\rangle$ involving the orbital magnetic moment $\mathcal{M}(\boldsymbol{k})$ (49, 50). Additionally, the P_3 tornado displays the extrinsic (intrinsic) helicity factor(s) pinpointedly under CP (LP) light pumping. This is understood as the intrinsic helicities are only transparent under the nonchiral LP light and otherwise, overridden by the extrinsic electric field rotation driving the electrons. These features constitute a perfect tomography of the defining helicity parameters of the surface-state system and the light–matter interaction, especially given the topological robustness characterized by W_s.

However, although tornadoes always exist in the spin-S_z signal P_3, their appearance in the vectorial orientation $\phi(\boldsymbol{k})$ of $\boldsymbol{P}_{\mathrm{in}}$ is intriguingly selective. Considering the nonequilibrium excitations due to the pumping, its winding number 2 presumably reflects the Berry phase contribution from both particle and hole. Most significantly, with other parameters provided, either W_s or w_ϕ is nonzero only for one type of CP light, making it an intriguing topological optical activity: dichroic $\mathbb{Z}_2$ topological switching between trivial and nontrivial nonequilibrium responses. Therefore, in addition to the helicity $\Xi_s = \pm 1$ dichroic switching of P_3, the $\mathbb{Z}_2$ $\boldsymbol{P}_{\mathrm{in}}$ response hints at further possibly interesting ultrafast spintronic applications taking advantage of the two types of all-optical two-state control.

In fact, the interplay between extrinsic and intrinsic factors can also be unmasked through the amplitude $|\boldsymbol{P}_{\mathrm{in}}|$, which exactly follows the response of P_3 except a doubled W_s, as exemplified in Fig. 3*B*. Unlike the P_3 response, aforementioned ϕ 's radial variation $\mathcal{K}$ is purely locked to ν, giving rise to a stable characterization of the sign of Dirac mass independent of any other factors. Lastly, in the case of negative spin-orbit coupling that reverses the sign of Fermi velocity v, only a sign change of $\boldsymbol{P}_{\mathrm{in}}$ is induced in the in-plane response that does not alter any topological features (51, 52).

The massless side of the phenomena is presumably simpler; every dichotomous response no longer exists if directly involving the mass sign ν, and only CP light remains active. The purely dichroic tornado in P_3 and $|\boldsymbol{P}_{\mathrm{in}}|$ persists. Vanishing mass, however, leads to singular π jump in the in-plane ϕ along the radial direction (e.g., Fig. 2 *A*, a2); the tornado trajectory of such a domain wall follows the driven dichroic helicity. ϕ 's variation (i.e., color rotation along the tornado arms) naturally inherits the intrinsic winding sense χ as in the massive case, although the do-

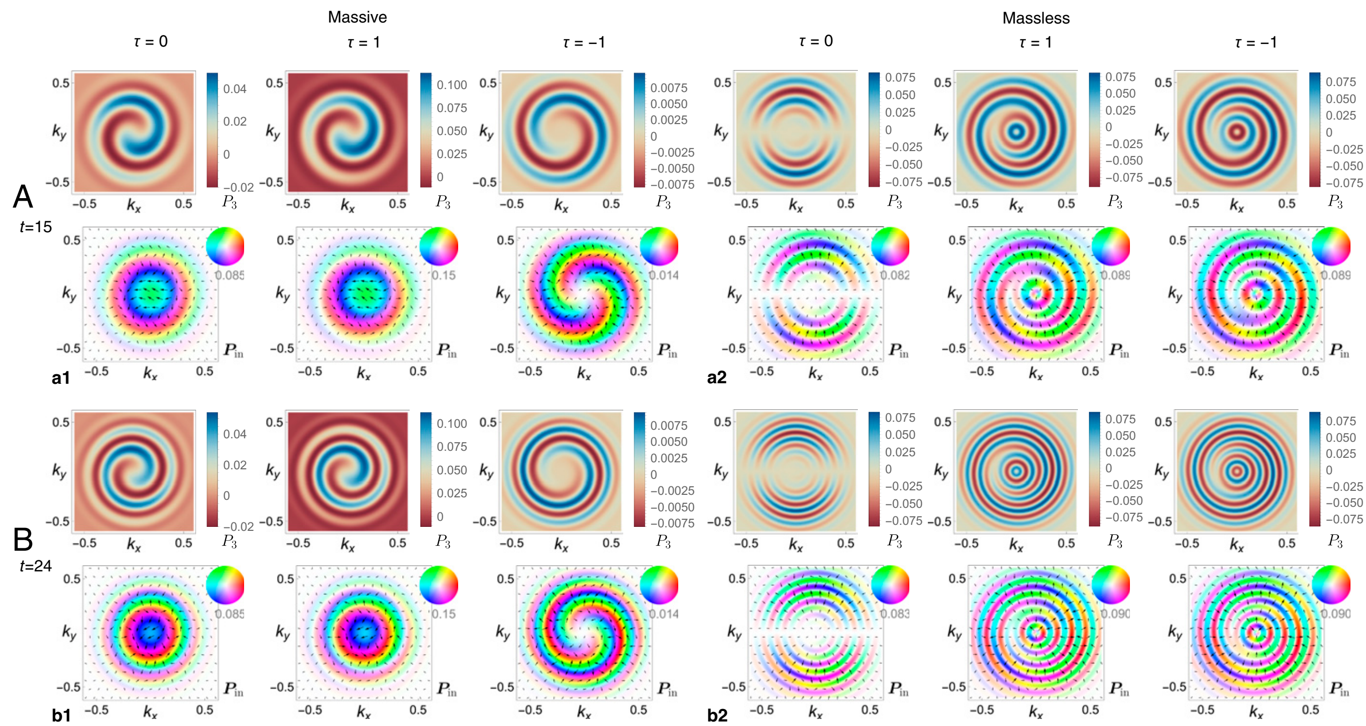

Fig. 2. Nonequilibrium tornado-like responses in the (k_x, k_y) plane. Equilibrium response subtracted SARPES signals [normal direction P_3 and in-plane $\boldsymbol{P}_{\text{in}} = (P_1, P_2)$] at (*A*) $t = 15$ and (*B*) $t = 24$ after the pump pulse. The energy cut at band midpoint $\varepsilon = 0$ is adopted without loss of generality. (*A*, a1 and *B*, b1) Positive mass ($\nu = 1$) and (*A*, a2 and *B*, b2) massless case for fixed surface-state helicity $\chi = 1$. Pump light dependence ($\tau = 0, \pm 1$ for LP along the x axis and right/left CP) is displayed across the columns. Scalar P_3 is plotted for spin-S_z signal. In-plane spin orientation angle $\phi = \tan^{-1} \boldsymbol{P}_{\text{in}}$ is plotted according to the rainbow color wheels in *Insets*; magnitude $|\boldsymbol{P}_{\text{in}}|$ is shown in opacity with maximal $|\boldsymbol{P}_{\text{in}}|$ indicated below each color wheel. Selected $\boldsymbol{P}_{\text{in}}$ vector arrows are shown with corresponding magnitude and orientation. Fig. 3*D* shows an enlarged illustration. Topological tornado-like spirals appear except for in the gapless case under LP light. As time elapses, from *A* to *B*, tornadoes evolve and rotate, and more tornado arms will be accommodated within a fixed $\boldsymbol{k}$-space region. Tornado responses as the distinguishing feature in relation to all three helicity factors are summarized in Table 1. Dichroic P_3 tornado switching helicity with different CP lights (*A*, a1 and *B*, b1; $\tau = \pm 1$ case of P_3) is in stark contrast to the $\mathbb{Z}_2$-like $\boldsymbol{P}_{\text{in}}$ tornado, which appears only under one particular CP light in the gapful case (*A*, a1 and *B*, b1; $\tau = -1$ case of $\boldsymbol{P}_{\text{in}}$). ϕ in the gapless case exhibits π jump, due to vanishing $\boldsymbol{P}_{\text{in}}$, along the radial direction once it goes across a spiral arm (*A*, a2 and *B*, b2; case of $\boldsymbol{P}_{\text{in}}$). Parameters are the same as in Fig. 1.

main wall prevents it from completing a quantized winding. The apparent distinction between the massive and massless responses is smoothly connected in the cross-over regime $|m|t \sim 1$. For instance, a tiny amount of magnetic doping ($|m|t \ll 1$) follows the massless behavior, and the late time response of finite doping ($|m|t \gg 1$) generally obeys the massive response pattern.

Physical Mechanism of Tornado. As seen previously, instead of the possible real transition, virtual excitations giving rise to off-diagonal coherence of electronic density matrix contribute to the tornado formation. On top of the ground-state spin momentum–locked concentric ring-like spin texture, we can intuitively view the optical pumping as producing a coherent $\boldsymbol{k}$-dependent matrix element and concomitant phase accumulation; the nontrivially correlated phase along the ring rotates the spins to yield the tornado. This in a way resembles the gas laser, where independent molecules are excited and brought in a correlated nontrivial coherence by the light working as glue. To gain quantitative insight into the nonequilibrium response, we resort to the Keldysh formalism to calculate the crucial $G^{<}(\boldsymbol{k}, t_1, t_2)$ and hence, the SARPES signal Eq. **3**. In this regard, the linear response is tractable and particularly useful as it captures leading virtual excitations but discards real transitions, given that the realistic pumping field is often well within the linear response regime. In addition, since the tornado response is of a stable topological nature, the features can persist even beyond as the above relatively larger field calculation confirms.

The analytical result matches the previous exact calculation in the linear response regime as it should. For the late time behavior of our main interest, we can derive an exceptionally simple expression for general two-band systems: $P_0^{(1)}(\varepsilon, \boldsymbol{k}, t) \equiv 0$ and

$$\boldsymbol{P}^{(1)}(\varepsilon, \boldsymbol{k}, t) = \frac{2A_0\, W(k)}{d^2}\left(f_{\varepsilon_{\boldsymbol{k}-}} - f_{\varepsilon_{\boldsymbol{k}+}}\right) F(\varepsilon)\tilde{\boldsymbol{P}}(\boldsymbol{k}, t) \quad \textbf{[6]}$$

with $f_{\varepsilon_{\boldsymbol{k}\pm}}$ the Fermi function for the upper and lower bands $\varepsilon_{\boldsymbol{k}\pm}$. The vanishing result in the density channel confirms the recovery of stable energy eigenstates after the pump's influence. For the spin channel, the dependence on occupation difference in the two bands indicates the optical inertness of both bands being empty or filled. The energy function in a Gaussian form $F(\varepsilon) = \mathrm{e}^{-(\varepsilon - d_0(k))^2 t_{\text{pb}}^2}$, where we include $d_0(k)$ for completeness, explains the aforementioned SARPES hot region. The energy range is limited by the probe pulse width; the signal is symmetric with respect to the band midpoint as a result of the interband quantum oscillation. The momentum envelope function takes a more complex form $W(k) = \sqrt{\frac{\pi}{2}}\, t_0 \mathrm{e}^{-2t_0^2(\Omega/2 - d(k))^2 - t_{\text{pb}}^2 d(k)^2}$ involving both the pump and probe; a disk-like signal centered at $k = 0$ can transform to an annulus-like one for large-enough Ω and t_0 (*SI Appendix*, Fig. S5 and note 2). These envelope functions also clarify that the absence or presence of resonant real pumping is inessential to the tornado signal up to minor modification, physically because the interested spin-channel signals rely on the interband coherent dynamics in virtual excitations rather than the real transitions. Finally, the time-dependent ($\boldsymbol{k}$ dependence suppressed and $\partial_j = \partial_{k_j}$)

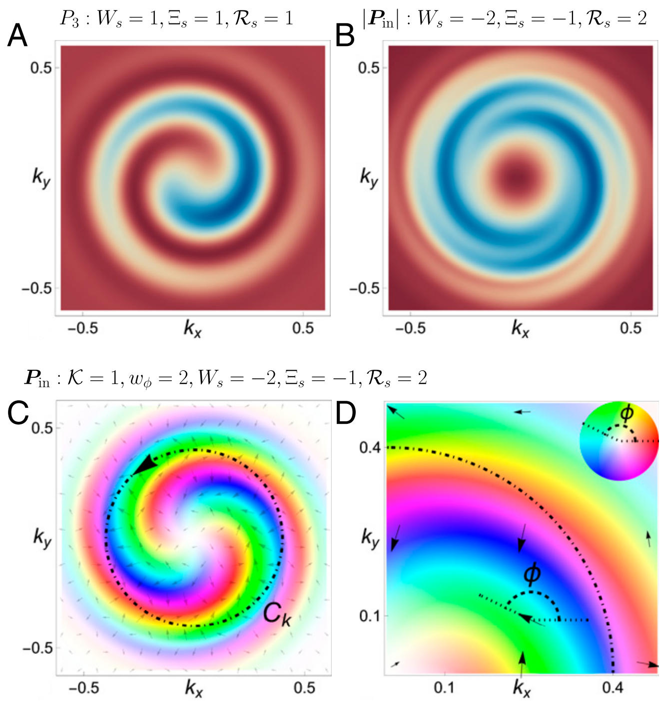

Fig. 3. Topological tornado indices illustrated in representative cases. Parameters are the same as in the Fig. 2 *A*, a1 massive case at $t = 15$. Scale legends are omitted for simplicity as they are unimportant for the robust tornado features. The spiral winding W_s is common for scalar signal (*A*) P_3 for $\tau = 1$ or (*B*) $|\boldsymbol{P}_{\rm in}|$ for $\tau = -1$ and vectorial in-plane signal (*C*) $\boldsymbol{P}_{\rm in}$ for $\tau = -1$. W_s determines the tornado spiral helicity $\Xi_s = \mathrm{sgn} W_s$ and the number $\mathcal{R}_s = |W_s|$ of repeating spiral arms. For the vectorial signal, more specific radial ordering $\mathcal{K}$ and azimuthal winding w_ϕ also exist and are combined to give W_s. *C* shows the counterclockwise circle C_k used in defining winding numbers. *D* zooms in on the upper right quadrant of *C* and exemplifies a particular vector $\boldsymbol{P}_{\rm in}$ and its orientation angle ϕ together with the rainbow color wheel in *D*, *Inset*.

$$\tilde{\boldsymbol{P}}(\boldsymbol{k},t) = d\,\{[\tau(d\,\partial_2\boldsymbol{d} - \boldsymbol{d}\,\partial_2 d) + \boldsymbol{d}\times\partial_1\boldsymbol{d}]\cos 2dt + [-(d\,\partial_1\boldsymbol{d} - \boldsymbol{d}\,\partial_1 d) + \tau\boldsymbol{d}\times\partial_2\boldsymbol{d}]\sin 2dt\} \quad [7]$$

solely accounts for all the features in Table 1. In fact, the scalar P_3 or $|\boldsymbol{P}_{\rm in}|$ admits a generic form

$$f(\boldsymbol{k})\sin[2nd(\boldsymbol{k})t + \theta_0 - \Theta(\boldsymbol{k})], \quad [8]$$

where $f(\boldsymbol{k}) > 0$, $n \in \mathbb{Z}_+$, and θ_0 is a constant. While it manifestly originates from the interband coherent oscillation at frequency $2d(\boldsymbol{k})$, the tornado at a given t is made possible since a proper relation between an increment of k and $\theta_{\boldsymbol{k}}$ can preserve the argument of sine. Exactly following Eq. **5**, the spiral winding number W_s is just given by the circular winding w_Θ of the angle $\Theta(\boldsymbol{k})$. Representatively, the dichroic P_3 tornado reads

$$\tilde{P}_3(\boldsymbol{k},t) = k(d(\boldsymbol{k}) + \chi\tau m)\sin[2d(\boldsymbol{k})t + \frac{\pi}{2} - \tau(\theta_{\boldsymbol{k}} + \chi\frac{\pi}{2})], \quad [9]$$

which perfectly explains its appearance in Table 1. The in-plane $\mathbb{Z}_2$ ϕ tornado bears a more delicate geometric explanation. The condition in Table 1 exactly specifies whether $\tilde{\boldsymbol{P}}_{\rm in}$ winds around the origin and hence, the trivial or topological winding (*Materials and Methods*). Correspondingly, $\tilde{\boldsymbol{P}}_{\rm in}$ crosses the origin only when $m = 0$ (i.e., the gap closes and hence, the singular behavior in the massless case), which is the topological transition point along the m axis.

To analytically glimpse into possible electronic real transition and nonlinear effects in general, we study as well the special case of a δ-pulse pump [e.g., $\boldsymbol{A}(t) = \tilde{A}_0\delta(t)\hat{x}$], which can account for an LP light ultrashort pump (*Materials and Methods*). The nonequilibrium part of SARPES signal reads

$$\begin{aligned} \delta P_0(\varepsilon,\boldsymbol{k}) &= cE_+(\varepsilon)d(\boldsymbol{k}) \\ \delta\boldsymbol{P}(\varepsilon,\boldsymbol{k},t) &= c\left[E_-(\varepsilon)\boldsymbol{d}(\boldsymbol{k}) + \bar{F}(\varepsilon)\boldsymbol{Z}(\alpha,t)\right], \end{aligned} \quad [10]$$

where $c = \frac{4\alpha(f_{\varepsilon_-} - f_{\varepsilon_+})}{(1+\alpha^2)^2 d^3}$, dimensionless $\alpha = ve\tilde{A}_0/2$ quantifies the deviation from equilibrium, $E_\pm(\varepsilon) = \alpha(d^2 - d_y^2)[F_+(\varepsilon) \mp F_-(\varepsilon)]$, the Gaussian $F_\pm(\varepsilon) = \mathrm{e}^{-(\varepsilon-\varepsilon_\pm)^2 t_{\rm pb}^2}$ from the resonant photoemission at two bands, $\bar{F}(\varepsilon) = \mathrm{e}^{-[(\varepsilon-d_0)^2 + d^2]t_{\rm pb}^2}$, and $\boldsymbol{Z}(\alpha,t)$ in the form of Eq. **8** encodes all linear and nonlinear tornado effects (*SI Appendix*, note 4). The time-independent $\delta P_0(\varepsilon,\boldsymbol{k})$ describes the result of real pumping from lower ε_- to higher ε_+. The time-dependent part in the spin channel not only matches Eq. **6** up to the linear response in α but also, suggests the same tornado topology even deep into the nonlinear regime, which can be confirmed from the exact response of short pump pulses. This partially supports the robust observation of tornado

Table 1. Correspondence between nonequilibrium topological tornado responses and three system helicity factors—intrinsic surface-state helicity $\chi = \pm 1$, sign of Dirac mass $\nu = \pm 1$ or massless case without ν, and extrinsic pump light helicity $\tau = 0, \pm 1$

		Massive		Massless	
Normal P_3 and in-plane $\lvert\boldsymbol{P}_{\rm in}\rvert$	Response strength	$\chi\nu\tau$	$\tau = \pm 1$	—	—
	Spiral winding W_s ($\times 2$ for $\lvert\boldsymbol{P}_{\rm in}\rvert$)	$\chi\nu$	$\tau = 0$	—	$\tau = 0$
		τ	$\tau = \pm 1$	τ	$\tau = \pm 1$
In-plane $\phi = \tan^{-1}(\boldsymbol{P}_{\rm in})$	Radial $\mathcal{K} = \mathrm{sgn}(\partial_k\phi)$	ν	—	—	—
	Circular winding w_ϕ	0	$\chi\nu\tau = 0, 1$	χ^*	$\tau = 0$
		2χ	$\chi\nu\tau = -1$		$\tau = \pm 1$
	Spiral winding $W_s = -\mathcal{K}w_\phi$	0	$\chi\nu\tau = 0, 1$	—	$\tau = 0$
		2τ	$\chi\nu\tau = -1$	τ^*	$\tau = \pm 1$

Spin-S_z signal $P_3(\boldsymbol{k})$ and in-plane signal amplitude $|\boldsymbol{P}_{\rm in}|$ show the same dichroism in both the strong or weak (± 1) response strength and the $\boldsymbol{k}$-space tornado helicity $\Xi_s = \mathrm{sgn} W_s = \pm 1$, although spiral winding W_s and hence, arm number $\mathcal{R}_s = |W_s|$ are doubled for $|\boldsymbol{P}_{\rm in}|$. The strength response combines all three factors; W_s is purely driven by extrinsic CP light, while it manifests intrinsic factors under LP light. (The massive case $|\boldsymbol{P}_{\rm in}|$ tornado can be less discernible in Fig. 2 due to obstruction from color but is otherwise observable when plotted separately [Fig. 3*B* and *SI Appendix*, Fig. S4].) In-plane vectorial tornado signal $\boldsymbol{P}_{\rm in}(\boldsymbol{k})$ contains more information than scalar signals. The azimuthal angle $\phi(\boldsymbol{k})$, encoding the in-plane orientational variation, exhibits a mass-only dependence of $\mathcal{K}$ along the radial direction. Two other related topological winding numbers w_ϕ, W_s exist in the massive case and exhibit a $\mathbb{Z}_2$ topological trivial–nontrivial switching for all three factors. W_s, common in both scalar and vectorial signals, is driven by CP light (τ) when tornado exists, as it shares the same physical meaning of describing spiral rotation. *The singular π-jump domain wall of ϕ, a double-armed helicity-τ tornado, disables $\mathcal{K}, w_\phi, W_s$ in the massless case; χ determines ϕ 's winding sense away from the domain wall for any light polarization.

topology for moderate strength well beyond the linear response regime and also hints that general pump pulses can eventually deviate from the linear response prediction of tornado topology at high-enough strength.

Discussion

To estimate realistic scales in connection to experiments, we introduce $k_0 = \varepsilon_0/v, \varepsilon_0$, the characteristic scales of wave number and energy, respectively. While ε_0 is typically given by the exchange gap $\Delta \sim 55\mathrm{meV}$ and hence, $k_0 \sim 0.03\text{Å}^{-1}$ with $v \sim 3\times10^5\mathrm{m/s}$ for instance, the driving frequency Ω can be more important for the gapless or nearly gapless case. The dimensionless strength of the pump pulse can be characterized by $\gamma = evA_0/\Omega$, which sensibly relates to the δ-pulse quantity $\alpha = \pi\gamma$. Existing experiments are estimated to fall well within linear response (e.g., $\gamma \sim 0.01$) (28, 31, 33) (*SI Appendix*, note 5). Exemplifying at $t = 0.5\mathrm{ps}$, the tornado arm width is $\sim 0.01\text{Å}^{-1}$. The femtosecond pump pulse frequency tunes widely from terahertz to visible; the ultrashort femtosecond probe pulse can provide time duration 0.02 to 0.5ps, energy resolution 5 to 100meV, and momentum resolution 0.004 to 0.01Å^{-1} that are able to observe the phenomena, given that SARPES signal strength proved to fall well within the experimental reach (5, 28, 31, 33, 35). For pump pulse width about the same order of light period $2t_0 \sim 2\pi/\Omega$ with, for example, $t_{\mathrm{pb}} \sim t_0$ and $\Omega \sim \Delta$, an example observation time window after the pump pulse could be 5 to $150t_0 \sim 0.2$ to 6ps. This is feasible in comparison with the experimental estimation of spin relaxation time at the order of 4 to 15ps (26, 31, 53). In *SI Appendix*, note 6, taking into account interaction effects, we discuss two relevant and related relaxation timescales; while the energy relaxation time is more easily measurable in experiments, the interband decoherence time plays a more important role in the phenomena of our interest. Fermi energy inside the gap is not essential since tornado signals persist outside the Fermi ring; finite temperature simply recovers signals inside (*SI Appendix*, Fig. S6). To observe and resolve conspicuous tornado signals in a disk region, shorter t_0, t_{pb}, and Ω not very far away from Δ can help but are not mandatory.

Our results show that the ultrafast spin-resolved response of the optically excited topological insulator surface state is an exceptionally apt platform of nonequilibrium topology, coherent quantum dynamics, and light–matter interaction. The topology of nonequilibrium spin textures in momentum space remains less addressed in quantum materials. Two-dimensional Rashba systems and the generalization to three-dimensional Weyl fermions as well as the spatially nonuniform cases are interesting problems left for future studies.

Materials and Methods

Model Hamiltonian and Time Evolution. We consider a general band electron Hamiltonian

$$\hat{H}_0 = \sum_{\boldsymbol{k}} \psi^\dagger(\boldsymbol{k}) H_0(\boldsymbol{k}) \psi(\boldsymbol{k}). \quad [11]$$

Writing in its tight-binding form for the original lattice model, interaction with a general external electromagnetic field $\boldsymbol{A}(\boldsymbol{r})$ can be derived from the Peierls substitution

$$\begin{aligned} &\sum_{\boldsymbol{r}\boldsymbol{r}'} \psi^\dagger(\boldsymbol{r}) H_0(\boldsymbol{r},\boldsymbol{r}')\, \mathrm{e}^{\mathrm{i}e\int_{\boldsymbol{r}'}^{\boldsymbol{r}} \mathrm{d}\boldsymbol{r}''\cdot\boldsymbol{A}(\boldsymbol{r}'')} \psi(\boldsymbol{r}') - \hat{H}_0 \\ &\approx \mathrm{i}e \sum_{\boldsymbol{k}\boldsymbol{k}'} \psi^\dagger(\boldsymbol{k}) \sum_{\boldsymbol{r}\boldsymbol{r}'} \mathrm{e}^{\mathrm{i}(\boldsymbol{k}_-\cdot\boldsymbol{r}_+ + \boldsymbol{k}_+\cdot\boldsymbol{r}_-)} H_0(\boldsymbol{r}_-)\boldsymbol{r}_- \cdot \boldsymbol{A}(\boldsymbol{r}_+)\psi(\boldsymbol{k}'), \\ &= e\sum_{\boldsymbol{k}\boldsymbol{k}'} \psi^\dagger(\boldsymbol{k}) \partial_{\boldsymbol{k}_+} H_0(\boldsymbol{k}_+)\cdot \boldsymbol{A}(\boldsymbol{k}_-)\psi(\boldsymbol{k}') \end{aligned} \quad [12]$$

where we denote $\boldsymbol{r}_- = \boldsymbol{r} - \boldsymbol{r}', \boldsymbol{r}_+ = \frac{\boldsymbol{r}+\boldsymbol{r}'}{2}$ and similarly, for $\boldsymbol{k}_\pm$. We use the fact that $H_0(\boldsymbol{r},\boldsymbol{r}')$ is periodic and approximate the Peierls phase by the midpoint-valued $\boldsymbol{A}$ accumulated along the path connecting the two sites, which is justified as the long-wavelength electromagnetic field is slowly varying at atomic scales. Therefore, in the optical long-wavelength limit of a spatially uniform time-dependent $\boldsymbol{A}(t)$, we obtain Eq. **2**.

The unitary time evolution can be performed via the EOM of the column field vector $\psi(t)$ in the Heisenberg picture

$$\mathrm{i}\dot{\psi}(t) = [\psi(t), \hat{H}^{\mathrm{H}}(t)], \quad [13]$$

where $\hat{H}^{\mathrm{H}}(t) = H_{\alpha\beta}(t)\psi^\dagger_\alpha(t)\psi_\beta(t)$, and we neglect $\boldsymbol{k}$ dependence for brevity. As required by the unitary time evolution of any operator $\psi_\alpha(t) = \hat{U}(t)\psi_\alpha\hat{U}^\dagger(t)$, the equal time canonical commutation relation should always hold:

$$\{\psi_\alpha(t), \psi^\dagger_\beta(t)\} = \delta_{\alpha\beta},\ \{\psi^\dagger_\alpha(t), \psi^\dagger_\beta(t)\} = \{\psi_\alpha(t), \psi_\beta(t)\} = 0. \quad [14]$$

We adopt the ansatz that attributes operator time dependence to a coefficient matrix $\psi_\alpha(t) = B_{\alpha\beta}(t)\psi_\beta$, which leads to a closed solution form for a quadratic Hamiltonian. In the present choice of the dynamical operators, we have the natural initial condition $B_{\alpha\beta}(-\infty) = \delta_{\alpha\beta}$. From Eq. **13**, we can derive an apparently nonlinear matrix EOM

$$\mathrm{i}\dot{B}(t) = B(t)M(t), \quad [15]$$

where $M(t) = B^\dagger(t)H(t)B(t)$ is Hermitian, and we use the canonical commutation relation for the time-independent Schrödinger operators. To ensure the validity of the ansatz, one can now verify the unitarity and hence, the general Eq. **14** by the invariant $B(t)B^\dagger(t) = \mathbb{I}$ as a consequence of the evolution, which can be proved from the initial condition and Eq. **15**. Under this situation, we reduce Eq. **15** to the matrix EOM

$$\mathrm{i}\dot{B}(t) = H(t)B(t) \quad [16]$$

that fully determines the time-dependent system and can be solved numerically.

The double-time Green's function with nonequilibrium information, introduced in the text, can be related to

$$G^<(\boldsymbol{k},t_1,t_2) = B(\boldsymbol{k},t_1)G_0^<(\boldsymbol{k})B^\dagger(\boldsymbol{k},t_2) \quad [17]$$

with the equilibrium Green's function

$$\begin{aligned} G_0^<(\boldsymbol{k}) &= \sum_{a=\pm} \mathrm{i}f_{\varepsilon_{\boldsymbol{k}a}}|\boldsymbol{k}a\rangle\langle\boldsymbol{k}a| \\ &= \frac{(\mathrm{e}^{-(d_0-\mu)\beta} + \cosh d\beta)\sigma_0 - \sinh d\beta\, \hat{\boldsymbol{d}}\cdot\boldsymbol{\sigma}}{-\mathrm{i}(2\cosh(d_0-\mu)\beta + 2\cosh d\beta)} \end{aligned} \quad [18]$$

specified from the band basis $|\boldsymbol{k}a\rangle$ using the Fermi distribution $f_{\boldsymbol{k}a} = (\mathrm{e}^{\beta(\varepsilon_{\boldsymbol{k}a}-\mu)}+1)^{-1}$ and given in Pauli decomposition form.

Keldysh Response Theory. In the time-contour (forward + branch and backward − branch) formalism of nonequilibrium Green's function, we have the Green's function matrix

$$\hat{G} = \begin{bmatrix} G^{++} & G^{+-} \\ G^{-+} & G^{--} \end{bmatrix} = \begin{bmatrix} G^{\mathbb{T}} & G^< \\ G^> & G^{\tilde{\mathbb{T}}} \end{bmatrix} \quad [19]$$

and the Keldysh rotated one

$$\check{G} = R\hat{G}R^\dagger = \begin{bmatrix} 0 & G^{\mathrm{a}} \\ G^{\mathrm{r}} & G^{\mathrm{k}} \end{bmatrix} \quad [20]$$

with $R = \frac{1}{\sqrt{2}}\begin{bmatrix} 1 & -1 \\ 1 & 1 \end{bmatrix}$. The Dyson equation $G = G_0(1+\Sigma G)$ holds for both cases where Keldysh-space matrix multiplication and argument convolution are understood. The corresponding self-energy matrices in the Keldysh space read in the present case as

$$\hat{\Sigma}(\boldsymbol{k},t;\boldsymbol{k}',t') = \Sigma_0\,\sigma_3, \quad \check{\Sigma}(\boldsymbol{k},t;\boldsymbol{k}',t') = \Sigma_0\,\sigma_1 \quad [21]$$

with $\Sigma_0 = H'(\boldsymbol{k}, t)\delta(\boldsymbol{k} - \boldsymbol{k}')\delta(t - t')$ and $H'(\boldsymbol{k}, t)$ the pumping interaction Hamiltonian we derived. From the exact Dyson equation of $G^<$,

$$G^< = (1 + G^r\Sigma^r)G_0^<(1 + \Sigma^a G^a) + G^r\Sigma^< G^a, \qquad [22]$$

we can obtain the linear response

$$G_1^< = G_0^<\Sigma_0 G_0^a + G_0^r\Sigma_0 G_0^<. \qquad [23]$$

As per our purpose, we evaluate $\mathscr{G}_i = \mathrm{Tr}[G_1^<\sigma_i]$ and derive the analytical form

$$\begin{aligned}&\mathscr{G}_i(\boldsymbol{k}, t_1, t_2)\\ &= \int_{-\infty}^{t_2} \mathrm{d}t A_\kappa(t) Y_i^\kappa(\boldsymbol{k}, t_+, t_-) - \int_{-\infty}^{t_1} \mathrm{d}t A_\kappa(t) Z_i^\kappa(\boldsymbol{k}, t_+, t_-),\end{aligned} \qquad [24]$$

where $\kappa = 1, 2, t_+ = t_1 + t_2 - 2t, t_- = t_1 - t_2$, and

$$\begin{aligned}Y_i^\kappa(\boldsymbol{k}, t_+, t_-) &= -\frac{\mathrm{e}^{-(d_0-\mu)\beta}X_i^\kappa + X_i^\kappa\big|_{t_\pm \to t_\pm - \mathrm{i}\beta}}{\cosh(d_0 - \mu)\beta + \cosh d\beta}\\ Z_i^\kappa(\boldsymbol{k}, t_+, t_-) &= -\frac{\mathrm{e}^{-(d_0-\mu)\beta}X_i^\kappa + X_i^\kappa\big|_{t_\pm \to t_\pm \pm \mathrm{i}\beta}}{\cosh(d_0 - \mu)\beta + \cosh d\beta}\end{aligned} \qquad [25]$$

with $d\mathrm{e}^{\mathrm{i}t_- d_0}X_i^\kappa(\boldsymbol{k}, t_+, t_-)$ given by $d(\partial^\kappa d_0 \cos dt_- - \mathrm{i}\hat{\boldsymbol{d}} \cdot \partial^\kappa \boldsymbol{d} \sin dt_-)$ when $i = 0$ and $-\mathrm{i}d_i\partial^\kappa d_0 \sin dt_- + (\boldsymbol{d} \times \partial^\kappa \boldsymbol{d})_i \sin dt_+ + d_i\hat{\boldsymbol{d}} \cdot \partial^\kappa \boldsymbol{d} \cos dt_- + (d\partial^\kappa d_i - d_i\hat{\boldsymbol{d}} \cdot \partial^\kappa \boldsymbol{d}) \cos dt_+$ when $i = 1, 2, 3$. Now, Eq. **24** can be evaluated analytically using a simple special function

$$\begin{aligned}I(\omega, a, T) =& \frac{1}{2}\int_{-\infty}^{T} \mathrm{d}\tau\, \mathrm{e}^{-\frac{\tau^2}{2t_0^2}} \mathrm{e}^{\mathrm{i}[\omega\tau + a(t-\tau)]}\\ =& \sqrt{\frac{\pi}{8}} t_0\, \mathrm{e}^{-\frac{t_0^2}{2}(\omega-a)^2} \mathrm{e}^{\mathrm{i}at} \left(1 + \mathrm{Erf}\left(\frac{T - \mathrm{i}(\omega - a)t_0^2}{\sqrt{2}t_0}\right)\right)\end{aligned} \qquad [26]$$

with $\omega = \pm\Omega, a = 2d, T = t_{1,2}$. We present the detailed relation in *SI Appendix*, note 2. This fully analytical theory of the double-time removal Green's function matches the exact numerical time evolution better and better toward the linear response regime (e.g., when $A_0 < 0.05$).

To elucidate the tornado responses, we especially focus on the late time behavior where the error function in Eq. **26** approaches unity when $T \gg t_0$. Now, Eq. **3** can be further evaluated analytically. We arrive at the most general form of the late time SARPES signal for a two-band model, $P_0^{((1))}(\varepsilon, \boldsymbol{k}, t) = 0$ and

$$\begin{aligned}&\boldsymbol{P}^{(1)}(\varepsilon, \boldsymbol{k}, t) = \frac{2A_0}{d}\left(f_{\varepsilon_-} - f_{\varepsilon_+}\right) F(\varepsilon) \times\\ &\{[\tau W_s(d\,\partial_2\boldsymbol{d} - \boldsymbol{d}\,\partial_2 d) + W_c\,\boldsymbol{d} \times \partial_1\boldsymbol{d}] \cos 2dt\\ &+ [-W_c(d\,\partial_1\boldsymbol{d} - \boldsymbol{d}\,\partial_1 d) + \tau W_s\,\boldsymbol{d} \times \partial_2\boldsymbol{d}] \sin 2dt\}\end{aligned} \qquad [27]$$

with $W_{c,s} = \sqrt{\frac{\pi}{2}} t_0 \mathrm{e}^{-d^2t_{\mathrm{pb}}^2} \sum_{a=\pm} a^x\, \mathrm{e}^{-\frac{t_0^2}{2}(a\Omega-2d)^2}$ where $x = 0, 1$ for $W_{c,s}$, respectively. Without affecting any topological features, one can approximate $W = W_{c,s} = \sqrt{\frac{\pi}{2}} t_0 \mathrm{e}^{-\frac{t_0^2}{2}(\Omega-2d)^2 - d^2t_{\mathrm{pb}}^2}$ and reach Eq. **6**.

Topological Tornado Response. The topological tornado information in Eq. **7** can be seen through simplification toward the general form Eq. **8** for the specific scenarios in a similar manner as Eq. **9**. For instance, when $\tau = 0$, we instead have ($\nu = 1$)

$$\begin{aligned}&\tilde{P}_3(\boldsymbol{k}, t) = \sqrt{m^2k_x^2 + d^2k_y^2}\\ &\times \sin\left[2dt + \frac{\pi}{2} - \nu\left(\chi \arctan(|m|k_x, dk_y) + \frac{\pi}{2}\right)\right].\end{aligned} \qquad [28]$$

Other situations are discussed in *SI Appendix*, note 3.

Now, we briefly sketch the proof of the $\mathbb{Z}_2$ orientational $\boldsymbol{P}_{\mathrm{in}}$ tornado. We decompose $-\tilde{\boldsymbol{P}}_{\mathrm{in}} = \boldsymbol{u} + \boldsymbol{v}$, where

$$\boldsymbol{u} = (\boldsymbol{k}_\tau \cdot \hat{\boldsymbol{q}})\,\boldsymbol{k}_\chi, \quad \boldsymbol{v} = m\begin{pmatrix} d + \chi\tau m & \\ & \chi\tau d + m\end{pmatrix}\hat{\boldsymbol{q}} \qquad [29]$$

with $\boldsymbol{k}_\pm = (\pm k_x, k_y)$, $\hat{\boldsymbol{q}} = (\cos 2dt, \sin 2dt)$. Given k (i.e., a circle C_k on the 2D $\boldsymbol{k}$ plane), $\boldsymbol{v}$ is a constant vector field. While $\boldsymbol{u}$ is oriented parallel to the radial direction of $\hat{\boldsymbol{k}}_\chi$, it vanishes at two diametrically opposite points on C_k where $\boldsymbol{k}_\tau \perp \hat{\boldsymbol{q}}$. In fact, the vector field $\boldsymbol{u}$ maps C_k to a new trajectory, a circle $\mathcal{C}_k$ that is doubly and χ clockwisely traversed and also passes the origin twice. For the translated circular trajectory $\mathscr{C}_k$ of $\tilde{\boldsymbol{P}}_{\mathrm{in}}$, a key observation is that as long as $m \neq 0, k > 0$,

$$\begin{cases}\tilde{\boldsymbol{P}}_{\mathrm{in}} = \boldsymbol{0} \text{ lies outside } \mathscr{C}_k & \tau = 0 \text{ or } \chi\tau\nu = 1\\ \tilde{\boldsymbol{P}}_{\mathrm{in}} = \boldsymbol{0} \text{ lies inside } \mathscr{C}_k & \chi\tau\nu = -1\end{cases}, \qquad [30]$$

which immediately dictates the $\mathbb{Z}_2$ response.

To see the robust correspondence to the sign of mass $\mathrm{sgn}(\partial_k\phi) = \nu$ in the in-plane orientational signal $\phi(\boldsymbol{k})$, we rely on the one-form $\mathrm{d}\phi = \frac{1}{|\tilde{P}_{\mathrm{in}}|^2}(\tilde{P}_x\mathrm{d}\tilde{P}_y - \tilde{P}_y\mathrm{d}\tilde{P}_x)$. In *SI Appendix*, note 3, we prove that $\frac{2d}{km}(\tilde{P}_x\partial_k\tilde{P}_y - \tilde{P}_y\partial_k\tilde{P}_x) > 0$ when $t > \frac{1}{2|m|}$ in general holds.

δ Pulse for LP Light. Note that δ pulse is not feasible to describe a CP light pulse since $\delta(t)$ automatically picks out one particular Hamiltonian at $t = 0$. For the LP light polarized along $\hat{x}$, we consider the Hermitian evolution generator $S = B^\dagger(0^-)H(0)B(0^-)$ for Eq. **15** for an infinitesimal pulse duration Δt, leading to

$$S\frac{\Delta t}{2}\Big|_{\Delta \to 0, \delta(t)\Delta t \to 1} = \frac{\alpha}{v}B^\dagger(0^-)\partial^1 H_0 B(0^-). \qquad [31]$$

It is crucial to make the δ-pulse evolution unitary, which can be achieved via the Padé approximant that divides the pulse into two parts (i.e., $t < 0$ and $t > 0$ parts). For the δ pulse, it suffices to apply the $R_{1,1}$ approximant (54)

$$B(0^+) = B(0^-)(I - \mathrm{i}S\frac{\Delta t}{2})(I + \mathrm{i}S\frac{\Delta t}{2})^{-1}. \qquad [32]$$

After the pulse, we have the time evolution $B(t) = U(t)B(0^+)$ with

$$U(t) = \mathrm{e}^{-\mathrm{i}H_0 t} = \mathrm{e}^{-\mathrm{i}d_0 t}\left(\cos dt\,\sigma_0 - \mathrm{i}\sin dt\,\hat{\boldsymbol{d}} \cdot \boldsymbol{\sigma}\right) \qquad [33]$$

since the time-dependent drive is off. Then, one can derive Eq. **10** (*SI Appendix*, note 4).

Data Availability. All study data are included in the article and/or *SI Appendix*.

ACKNOWLEDGMENTS. X.-X.Z. appreciates discussion with L. Schwarz, Y. Fan, J. J. He, I. Belopolski, A. F. Kemper, and J. K. Freericks. This work was supported by Japan Society for the Promotion of Science KAKENHI grant 18H03676 and Core Research for Evolutional Science and Technology, Japan Science and Technology Agency grants JPMJCR16F1 and JPMJCR1874. X.-X.Z. was partially supported by the RIKEN Special Postdoctoral Researcher Program.

1. C. Giannetti *et al.*, Ultrafast optical spectroscopy of strongly correlated materials and high-temperature superconductors: A non-equilibrium approach. *Adv. Phys.* **65**, 58–238 (2016).
2. D. Nicoletti, A. Cavalleri, Nonlinear light–matter interaction at terahertz frequencies. *Adv. Opt. Photonics* **8**, 401–464 (2016).
3. C. L. Smallwood *et al.*, Tracking Cooper pairs in a cuprate superconductor by ultrafast angle-resolved photoemission. *Science* **336**, 1137–1139 (2012).
4. N. Gedik, I. Vishik, Photoemission of quantum materials. *Nat. Phys.* **13**, 1029–1033 (2017).
5. J. A. Sobota, Y. He, Z. X. Shen, Angle-resolved photoemission studies of quantum materials. *Rev. Mod. Phys.* **93**, 025006 (2021).
6. S. Loth, M. Etzkorn, C. P. Lutz, D. M. Eigler, A. J. Heinrich, Measurement of fast electron spin relaxation times with atomic resolution. *Science* **329**, 1628–1630 (2010).
7. T. L. Cocker *et al.*, An ultrafast terahertz scanning tunnelling microscope. *Nat. Photonics* **7**, 620–625 (2013).

8. M. Eisele *et al.*, Ultrafast multi-terahertz nano-spectroscopy with sub-cycle temporal resolution. *Nat. Photonics* **8**, 841–845 (2014).
9. M. Mitrano et al., Possible light-induced superconductivity in K_3C_{60} at high temperature. *Nature* **530**, 461–464 (2016).
10. O. Ostroverkhova, Organic optoelectronic materials: Mechanisms and applications. *Chem. Rev.* **116**, 13279–13412 (2016).
11. D. N. Basov, R. D. Averitt, D. Hsieh, Towards properties on demand in quantum materials. *Nat. Mater.* **16**, 1077–1088 (2017).
12. Y. Tokura, M. Kawasaki, N. Nagaosa, Emergent functions of quantum materials. *Nat. Phys.* **13**, 1056–1068 (2017).
13. M. Z. Hasan, C. L. Kane, Colloquium: Topological insulators. *Rev. Mod. Phys.* **82**, 3045–3067 (2010).
14. X. L. Qi, S. C. Zhang, Topological insulators and superconductors. *Rev. Mod. Phys.* **83**, 1057–1110 (2011).
15. M. Neupane *et al.*, Gigantic surface lifetime of an intrinsic topological insulator. *Phys. Rev. Lett.* **115**, 116801 (2015).
16. Y. L. Chen *et al.*, Massive Dirac fermion on the surface of a magnetically doped topological insulator. *Science* **329**, 659–662 (2010).
17. C. Z. Chang *et al.*, Experimental observation of the quantum anomalous Hall effect in a magnetic topological insulator. *Science* **340**, 167–170 (2013).
18. Y. Tokura, K. Yasuda, A. Tsukazaki, Magnetic topological insulators. *Nat. Rev. Phys* **1**, 126–143 (2019).
19. P. Wang *et al.*, Intrinsic magnetic topological insulators. *Innovation (N Y)* **2**, 100098 (2021).
20. A. Kirilyuk, A. V. Kimel, T. Rasing, Ultrafast optical manipulation of magnetic order. *Rev. Mod. Phys.* **82**, 2731–2784 (2010).
21. A. Kirilyuk, A. V. Kimel, T. Rasing, Laser-induced magnetization dynamics and reversal in ferrimagnetic alloys. *Rep. Prog. Phys.* **76**, 026501 (2013).
22. D. Hsieh *et al.*, A tunable topological insulator in the spin helical Dirac transport regime. *Nature* **460**, 1101–1105 (2009).
23. N. Xu, H. Ding, M. Shi, Spin- and angle-resolved photoemission on the topological Kondo insulator candidate: SmB6. *J. Phys. Condens. Matter* **28**, 363001 (2016).
24. Y. H. Wang, H. Steinberg, P. Jarillo-Herrero, N. Gedik, Observation of Floquet-Bloch states on the surface of a topological insulator. *Science* **342**, 453–457 (2013).
25. T. Oka, S. Kitamura, Floquet engineering of quantum materials. *Annu. Rev. Condens. Matter Phys.* **10**, 387–408 (2019).
26. P. Hosur, Circular photogalvanic effect on topological insulator surfaces: Berry-curvature-dependent response. *Phys. Rev. B Condens. Matter Mater. Phys.* **83**, 035309 (2011).
27. J. W. McIver, D. Hsieh, H. Steinberg, P. Jarillo-Herrero, N. Gedik, Control over topological insulator photocurrents with light polarization. *Nat. Nanotechnol.* **7**, 96–100 (2011).
28. J. Reimann *et al.*, Subcycle observation of lightwave-driven Dirac currents in a topological surface band. *Nature* **562**, 396–400 (2018).
29. J. Yu *et al.*, Helicity-dependent photocurrent of the top and bottom Dirac surface states of epitaxial thin films of three-dimensional topological insulators Sb_2Te_3. *Phys. Rev. B* **100**, 235108 (2019).
30. M. Schüler *et al.*, Local Berry curvature signatures in dichroic angle-resolved photoelectron spectroscopy from two-dimensional materials. *Sci. Adv.* **6**, eaay2730 (2020).
31. C. Cacho *et al.*, Momentum-resolved spin dynamics of bulk and surface excited states in the topological insulator Bi_2Se_3. *Phys. Rev. Lett.* **114**, 097401 (2015).
32. P. Zhang *et al.*, Observation of topological superconductivity on the surface of an iron-based superconductor. *Science* **360**, 182–186 (2018).
33. C. Jozwiak *et al.*, Spin-polarized surface resonances accompanying topological surface state formation. *Nat. Commun.* **7**, 13143 (2016).
34. Z. Nie *et al.*, Spin-ARPES EUV beamline for ultrafast materials research and development. *Appl. Sci. (Basel)* **9**, 370 (2019).
35. B. Lv, T. Qian, H. Ding, Angle-resolved photoemission spectroscopy and its application to topological materials. *Nat. Rev. Phys* **1**, 609–626 (2019).
36. L. Fu, Hexagonal warping effects in the surface states of the topological insulator Bi_2Te_3. *Phys. Rev. Lett.* **103**, 266801 (2009).
37. C. X. Liu *et al.*, Model Hamiltonian for topological insulators. *Phys. Rev. B Condens. Matter Mater. Phys.* **82**, 045122 (2010).
38. M. Cattelan, N. A. Fox, A perspective on the application of spatially resolved ARPES for 2D materials. *Nanomaterials (Basel)* **8**, 284 (2018).
39. P. S. Keatley *et al.*, A platform for time-resolved scanning Kerr microscopy in the near-field. *Rev. Sci. Instrum.* **88**, 123708 (2017).
40. E. J. McCormick *et al.*, Imaging spin dynamics in monolayer WS_2 by time-resolved Kerr rotation microscopy. *2D Mater.* **5**, 011010 (2017).
41. S. Yamamoto *et al.*, Femtosecond resonant magneto-optical Kerr effect measurement on an ultrathin magnetic film in a soft x-ray free electron laser. *Jpn. J. Appl. Phys.* **57**, 09TD02 (2018).
42. A. Kamenev, *Field Theory of Non-Equilibrium Systems* (Cambridge University Press, Cambridge, United Kingdom, 2009).
43. G. Stefanucci, R. van Leeuwen, *Nonequilibrium Many-Body Theory of Quantum Systems* (Cambridge University Press, New York, NY, 2015).
44. J. K. Freericks, H. R. Krishnamurthy, T. Pruschke, Theoretical description of time-resolved photoemission spectroscopy: Application to pump-probe experiments. *Phys. Rev. Lett.* **102**, 136401 (2009).
45. A. Kemper, O. Abdurazakov, J. Freericks, General principles for the nonequilibrium relaxation of populations in quantum materials. *Phys. Rev. X* **8**, 041009 (2018).
46. J. K. Freericks, H. R. Krishnamurthy, M. A. Sentef, T. P. Devereaux, Gauge invariance in the theoretical description of time-resolved angle-resolved pump/probe photoemission spectroscopy. *Phys. Scr. T* **165**, 014012 (2015).
47. J. Freericks, H. Krishnamurthy, Constant matrix element approximation to time-resolved angle-resolved photoemission spectroscopy. *Photonics* **3**, 58 (2016).
48. D. Xiao, M. C. Chang, Q. Niu, Berry phase effects on electronic properties. *Rev. Mod. Phys.* **82**, 1959–2007 (2010).
49. I. Souza, D. Vanderbilt, Dichroicf-sum rule and the orbital magnetization of crystals. *Phys. Rev. B Condens. Matter Mater. Phys.* **77**, 054438 (2008).
50. W. Yao, D. Xiao, Q. Niu, Valley-dependent optoelectronics from inversion symmetry breaking. *Phys. Rev. B Condens. Matter Mater. Phys.* **77**, 235406 (2008).
51. X. L. Sheng *et al.*, Topological insulator to Dirac semimetal transition driven by sign change of spin-orbit coupling in thallium nitride. *Phys. Rev. B Condens. Matter Mater. Phys.* **90**, 245308 (2014).
52. S. Nie, G. Xu, F. B. Prinz, S. C. Zhang, Topological semimetal in honeycomb lattice LnSI. *Proc. Natl. Acad. Sci. U.S.A.* **114**, 10596–10600 (2017).
53. V. Iyer, Y. Chen, X. Xu, Ultrafast surface state spin-carrier dynamics in the topological insulator Bi_2Te_2Se. *Phys. Rev. Lett.* **121**, 026807 (2018).
54. W. H. Press, S. A. Teukolsky, W. T. Vetterling, B. P. Flannery, *Numerical Recipes: The Art of Scientific Computing* (Cambridge University Press, Cambridge, United Kingdom, ed. 3, 2007).